

Article

Experimental Study on the Influence of Bulbous Bow Form on the Velocity Field around the Bow of a Trimaran Using Towed Underwater 2D-3C SPIV

Rui Deng ^{1,2}, Shigang Wang ^{1,2}, Wanzhen Luo ^{1,2} and Tiecheng Wu ^{1,2,*} 

¹ School of Marine Engineering and Technology, Sun Yat-sen University, Zhuhai 518000, China; dengr23@mail.sysu.edu.cn (R.D.); wangshg5@mail2.sysu.edu.cn (S.W.); luowzh5@mail.sysu.edu.cn (W.L.)
² Southern Marine Science and Engineering Guangdong Laboratory (Zhuhai), Zhuhai 519082, China
* Correspondence: wutch7@mail.sysu.edu.cn; Tel.: +86-187-4514-7797

Abstract: In this study, particle image velocimetry was applied to measure the flow field around the bow region of a trimaran with different appendages. The dimensionless axial velocity u/U in test planes 1 and 2 of the testing model was measured by using a towed underwater stereoscopic particle image velocimetry (SPIV) system. Based on the measured flow field data, the local sinkage values in test planes 1 and 2 of the testing model with different appendages at speeds of 1.766 and 2.943 m/s were presented. In addition, the effects of speed, bulbous bow type, T foils, and bow wave on the axial velocity u/U were studied in detail. The acquired experimental data help in understanding the distribution of the flow field around the ship bow, and the data can also act as a reference to verify computational fluid dynamics (CFD) results.

Keywords: stereo particle image velocimetry; towing tank experiment; flow field around the bulbous bow; hydrodynamic appendages; bow wave



Citation: Deng, R.; Wang, S.; Luo, W.; Wu, T. Experimental Study on the Influence of Bulbous Bow Form on the Velocity Field around the Bow of a Trimaran Using Towed Underwater 2D-3C SPIV. *J. Mar. Sci. Eng.* **2021**, *9*, 905. <https://doi.org/10.3390/jmse9080905>

Academic Editor: Kamal Djidjeli

Received: 15 July 2021

Accepted: 17 August 2021

Published: 21 August 2021

Publisher's Note: MDPI stays neutral with regard to jurisdictional claims in published maps and institutional affiliations.



Copyright: © 2021 by the authors. Licensee MDPI, Basel, Switzerland. This article is an open access article distributed under the terms and conditions of the Creative Commons Attribution (CC BY) license (<https://creativecommons.org/licenses/by/4.0/>).

1. Introduction

Due to the influence of the bow geometry, the type of appendages, the bow wave, and the three-dimensional flow separation, the flow field around the bow is complex. When a ship moves, the bow of the hull interacts with the water first, and as an important part of the flow field around the ship, the flow field of the bow is closely related to the ship's resistance performance, seakeeping performance, vibration, and noise performance. The application of flow field measurement technology to measure the flow field around the bow region of a ship and optimize and design the bow and appendages based on the measured flow field is important for improving ship resistance, seakeeping, vibration, and noise performance. As an advanced flow field measurement technology, particle image velocimetry (PIV) is widely used in the measurement of the flow fields around ships and marine structures. The assembly mode of the towing tank PIV measurement system has changed from the fixed mode of the tank quay wall to the towing mode with the carriage. In addition, the analytical capability of the flow field parameters has changed from two-dimensional two-component (2D-2C) to three-dimensional three-component (3D-3C) [1–5]. Extensive research has significantly contributed to revealing the flow characteristics of the flow field around the stern [6–12]. This paper investigates the velocity field around the bow of a trimaran using towed underwater two-dimensional three-component stereoscopic particle image velocimetry (2D-3C SPIV) and then reviews the literature on the measurements and distributions of the flow field around the ship bow.

Newman [13], Hirata [14], and Oertel [15] carried out a simple type of ship bow flow field analysis based on the analytical fluid dynamics method under direct and yaw conditions. Grosenbaugh et al. [16,17] researched the simplified two-dimensional flow field around the bow of a ship using experimental observation methods. Fry et al. [18] applied

a three-dimensional towing tank Laser Doppler Velocimetry (LDV) system to measure the velocity field around the bow of a Series 60, Block 60 ship model and a high-speed surface ship with a bulbous bow configuration; the flow characteristics around the bow were analyzed based on the measured crossflow vector and streamwise contour data in different transverse and longitudinal planes. Maruo et al. [19] experimentally measured the free surface phenomena around the bow of simple wedge-shaped models in the towing tank and analyzed the free surface flow around the bow. Longo [20] and Toda et al. [21,22] measured the mean flow in the boundary layers, wake fields, and wave fields of a Series 60 Block coefficient (CB) = 0.6 ship model for Froude numbers 0.16 and 0.316 using a 5-hole pitot probe and pressure transducers. Stern et al. [23] carried out a CFD numerical study of the bow flow of a Series 60 CB = 0.6 ship model and compared it with experimental data. After that, Longo et al. [24] and Tahara et al. [25] conducted experiments on and numerical analysis of the boundary layers, wake fields, and wave fields for a Series 60 CB = 0.6 ship model in steady drift motion. Katz et al. [26,27] measured the flow field structure of the bow wave of a ship model using 2D PIV in the towing tank. Mallat et al. [28,29] measured the flow field at the longitudinal section in the bow region of a ship with a reduction ratio of 1/30 and used a 2D PIV measurement system in a circulating water tank. Cozijn et al. [30] used the 2D-3C SPIV measurement system to measure and study the flow field around the bow thrust area of a dynamically positioned ship in the tank of Marine Research Institute Netherland (MARIN). Yoon et al. [31] used the towed underwater tomographic particle image velocimetry (TPIV) system to measure and analyze the flow field around David Taylor Model Basin (DTMB) model 5415 under straight-ahead and static drift 10° and 20° conditions, and the measurement sections included the bow region. Bhushan et al. [32,33] conducted a CFD numerical simulation of DTMB model 5415 around the flow field and compared it with experimental measurements. Jacobi et al. [34] used 2D-3C SPIV to perform multi-plane PIV measurements on the velocity field around the bow of a fast ship at speeds up to Froude number (Fr) 0.8 and performed pressure reconstruction based on the obtained velocity information.

Although this series of studies on flow fields around the bow areas of ships have obtained some flow field data, to the best of our knowledge, experimental data on the flow field around a ship's bow are still lacking and limited, and any related measurements will be useful to the marine engineering research community at large. The acquired experimental data can help understand the distribution of the flow field around the ship's bow, and the data can also be a reference to verify CFD results.

In this experimental study, the dimensionless axial velocity u/U in test planes 1 and 2 of a trimaran with different appendages was measured and studied by a towed underwater SPIV system. The influence of a bulbous bow type, T foils, and a bow wave on axial velocity distribution was the main concern. The content of this paper is organized as follows: Section 2 describes the geometric model and experimental conditions. Section 3 presents the trim and sinkage of the hull with different appendages. The experimental setup is illustrated in detail in Section 4, which includes three subsections: Facility and SPIV System, Test Details, and Analysis of the Velocity Field. Measurement results under different conditions are illustrated in detail in Section 5. In particular, Section 5.1 reports the influence of a bulbous bow type on the axial velocity distribution. The influence of T foils on the axial velocity distribution is described in Section 5.2, and Section 5.3 discusses the influence of a bow wave on the axial velocity distribution. Section 6 delivers the conclusions of this study.

2. Geometric Model and Experimental Conditions

2.1. Experimental Modes

The experimental model used in this study was a trimaran with a center hull, two outriggers, and some appendages. Different views of the geometric model of the trimaran are shown in Figure 1. The same model was used in an experimental and numerical study on seakeeping performance by Deng et al. [35], and the detail lines plan and configuration

of the test model were presented in this reference. The main parameters of the trimaran are shown in Table 1. The interval between the central longitudinal planes of the center hull and the outrigger of this trimaran was 0.42 m. To weaken the reflection of the laser on the hull surface when performing experimental measurements, the surface in the measurement area of the ship bow was painted matte black. The local right-hand Cartesian coordinate system used in this PIV measurement experiment was located at the intersection of the ship bow, the water-line plane, and the central longitudinal plane (see Figure 1).

Table 1. Main parameters of the testing model.

| Principal Hull Data | | Center Hull | Outrigger |
|------------------------------------|----------|-------------|-----------|
| Length between perpendiculars (m) | L_{pp} | 3.60 | 1.25 |
| Breadth (m) | B | 0.28 | 0.05 |
| Draft (m) | T | 0.13 | 0.04 |
| Displacement (kg) | Δ | 73.10 | 1.05 |
| Wet surface area (m ²) | S | 0.84 | 0.05 |

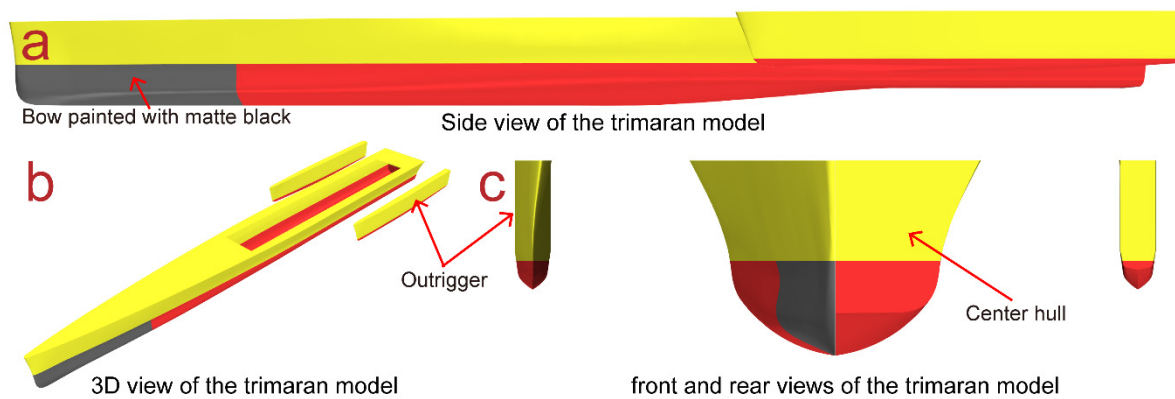


Figure 1. Geometric model of the testing trimaran: (a) side view of the trimaran model, (b) 3D view of the trimaran model, and (c) front and rear views of the trimaran model.

The bulbous bow and T foils assembled in the experimental model are shown in Figure 2. Figure 2a displays the schematic diagram of the assembly position of the bulbous bow and T foils. Figure 2b shows the basic bulbous bow, Figure 2c the T foils, and Figure 2d the testing model with different appendages. A similar bulbous bow and similar T foils are also presented in references [36–38]. The length l , maximum width b , and maximum thickness t of the basic bulbous bow were 322.6, 29.6, and 59.3 mm, respectively. The large bulbous bow is the basic one installed on the baseline of the hull, and its stern tip coincides with the 19 stations. The small bulbous bow is obtained by moving the large one to the vertical and longitudinal positions. The distance D from the axis of the small bulbous bow to the baseline of the hull was 120.0 mm, and the longitudinal distance F from the large bulbous bow was 60.0 mm. The profile of the hydrofoil and T foils pillar was airfoil 0012 of National Advisory Committee for Aeronautics (NACA 0012). The chord length of the pillar section was 37.5 mm, the hydrofoil span St was 144.0 mm, the maximum chord length C_1 was 90.8 mm, and the minimum chord length C_2 was 72.9 mm. The distance between the trailing edge of the hydrofoil pillar of T foils and the bow post was 189.8 mm.

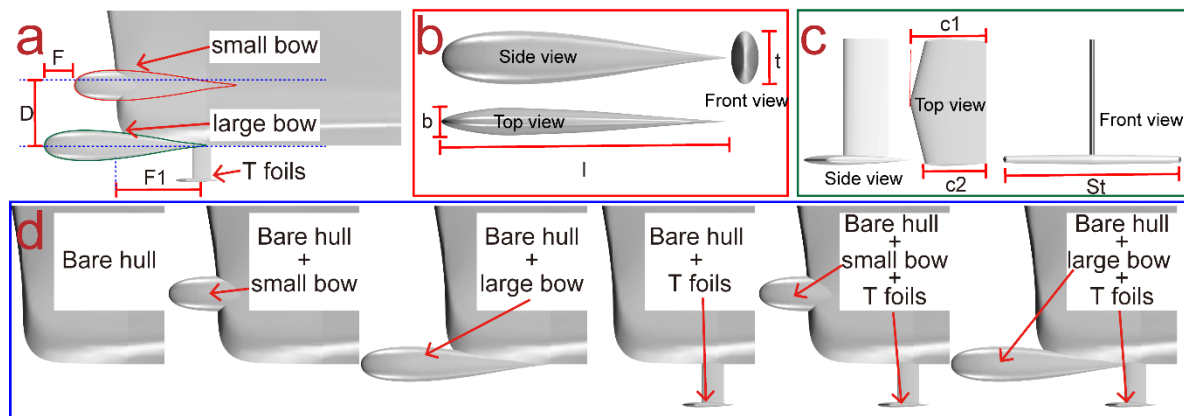


Figure 2. Bulbous bow and T foils assembled in the experimental model: (a) schematic diagram of the assembly position of the bulbous bow and T foils, (b) basic bulbous bow, (c) T foils, and (d) testing model with different appendages.

2.2. Experimental Conditions

The testing conditions, including test planes, draft, and speed, for measuring the velocity field around the bow are shown in Table 2 and Figure 3. The experimental planes of the flow fields were test planes 1 and 2 located at $X/L_{pp} = 0.0167$ and 0.0611 , respectively.

Table 2. PIV test conditions.

| Testing Conditions | Unit | Parameters |
|----------------------|------|---------------------|
| Test plane-1 | - | $X/L_{pp} = 0.0167$ |
| Test plane-2 | - | $X/L_{pp} = 0.0611$ |
| Draft of center hull | m | 0.13 |
| Draft of outrigger | m | 0.04 |
| Fluid medium | - | Water |
| Test speed | m/s | 1.766, 2.943 |
| Wave conditions | - | Clam water |

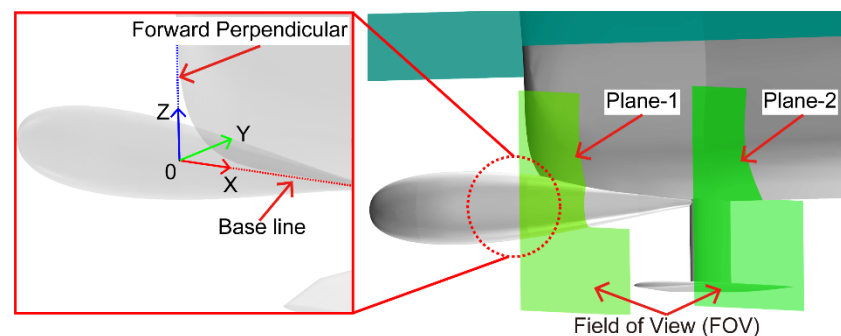


Figure 3. Test planes and FOV draft, and speed for measuring the velocity field around the bow.

3. Trim and Sinkage of the Hull with Different Appendages

The hydrodynamic appendages, such as the bulbous bow and T foils, assembled in the bow area of the hull often have corresponding effects on the wake field and stable navigation posture of the ship. Before PIV measurement of the flow field around the bow, we used a four-component motion measurement device to measure the sinkage and trim of the ship equipped with different hydrodynamic appendages. The corresponding measured values of sinkage and trim are shown in Table 3. The values of the sinkage and trim of the hull in the static floating state were 0 mm and 0° , respectively. The positive value of sinkage indicates that the vertical posture of the ship is raised, and the positive value of the trim indicates that the ship is in the bowing state.

Table 3. Experimental values of the sinkage and trim of the testing model.

| Testing Model | Sinkage (mm) | | Trim (°) | |
|------------------------------------------------|--------------|-----------|-----------|-----------|
| | 1.766 m/s | 2.943 m/s | 1.766 m/s | 2.943 m/s |
| Bare hull | −3.761 | −13.360 | 0.008 | 0.544 |
| Bare hull with a small bulbous bow | −3.840 | −13.160 | 0.013 | 0.559 |
| Bare hull with a large bulbous bow | −3.680 | −13.160 | 0.006 | 0.498 |
| Bare hull with T foils | −4.077 | −13.724 | −0.020 | 0.483 |
| Bare hull with a small bulbous bow and T foils | −4.149 | −13.665 | −0.017 | 0.519 |
| Bare hull with a large bulbous bow and T foils | −4.180 | −13.739 | −0.008 | 0.431 |

The sinkage of a ship usually refers to the vertical movement at the center of gravity of the hull. Since the measurement planes of PIV are not at the center of gravity of the hull, it was necessary to convert the local sinkage value at test plane 1 using the distance between test plane 1 and the center of gravity and the trim angle of the ship. The local sinkage values at test planes -1 and -2 ($Z_{\text{plane-1}}$ and $Z_{\text{plane-2}}$) were computed as follows:

$$\begin{aligned} Z_{\text{plane-1}} &= Z_{\text{sinkage}} + \Delta Z_{\text{Trim}} \\ &= Z_{\text{sinkage}} + \left(\frac{1}{2} - 0.00167\right) L_{\text{pp}} \times \tan \theta \end{aligned} \tag{1}$$

$$\begin{aligned} Z_{\text{plane-2}} &= Z_{\text{sinkage}} + \Delta Z_{\text{Trim}} \\ &= Z_{\text{sinkage}} + \left(\frac{1}{2} - 0.0611\right) L_{\text{pp}} \times \tan \theta \end{aligned} \tag{2}$$

where Z_{sinkage} is the value of vertical movement at the center of gravity of the hull, ΔZ_{Trim} is the value of vertical movement at test planes 1 and 2 caused by the trim of the hull, θ is the ship’s trim angle, and L_{pp} is the length between perpendiculars. The local sinkage value at test plane 1 of the testing model at speeds of 1.766 and 2.943 m/s are shown in Table 4, and the local sinkage value at test plane 2 of the testing model at a speed of 1.766 m/s are shown in Table 5.

Table 4. Local sinkage value at test plane 1 of the testing model at speeds of 1.766 and 2.943 m/s.

| Testing Model | 1.766 m/s | | | 2.943 m/s | | |
|------------------------------------------------|----------------------------------|-------------------------------|---------------------------|----------------------------------|-------------------------------|---------------------------|
| | $\Delta Z_{\text{sinkage}}$ (mm) | ΔZ_{trim} (mm) | $Z_{\text{plane-1}}$ (mm) | $\Delta Z_{\text{sinkage}}$ (mm) | ΔZ_{trim} (mm) | $Z_{\text{plane-1}}$ (mm) |
| Bare hull | −3.761 | 0.243 | −3.518 | −13.360 | 16.512 | 3.152 |
| Bare hull with a small bulbous bow | −3.840 | 0.395 | −3.445 | −13.160 | 16.967 | 3.807 |
| Bare hull with a large bulbous bow | −3.680 | 0.182 | −3.498 | −13.160 | 15.115 | 1.955 |
| Bare hull with T foils | −4.077 | −0.607 | −4.684 | −13.724 | 14.660 | 0.936 |
| Bare hull with a small bulbous bow and T foils | −4.149 | −0.516 | −4.665 | −13.665 | 15.753 | 2.088 |
| Bare hull with a large bulbous bow and T foils | −4.180 | −0.243 | −4.423 | −13.739 | 13.082 | −0.657 |

Table 5. Local sinkage value at test plane 2 of the testing model at a speed of 1.766 m/s.

| Testing Model | 1.766 m/s | | |
|------------------------------------------------|----------------------------------|-------------------------------|---------------------------|
| | $\Delta Z_{\text{sinkage}}$ (mm) | ΔZ_{trim} (mm) | $Z_{\text{plane-2}}$ (mm) |
| Bare hull | −3.761 | 0.221 | −3.540 |
| Bare hull with T foils | −4.077 | −0.551 | −4.628 |
| Bare hull with a small bulbous bow and T foils | −4.149 | −0.469 | −4.618 |
| Bare hull with a large bulbous bow and T foils | −4.180 | −0.221 | −4.401 |

4. Experimental Setup

4.1. Facility and SPIV System

The velocity field around the bow of a trimaran with different appendages was measured in the towing tank (108 m long, 7 m wide, and 3.5 m deep) at Harbin Engineering University, China. The SPIV system used in this study was a customized stereoscopic underwater PIV system for towing tanks (Dantec Dynamics Inc., Skovlunde, Denmark). The submersible PIV system, comprising submersible camera modules, mirror modules, and a submersible light sheet unit, has two configurations, asymmetrical and symmetrical. The configuration used in this study was asymmetrical. The image acquisition system was composed of two FlowSense 4M Mk II 12-bit precision charge coupled device (CCD) cameras (Dantec Dynamics Inc., Skovlunde, Denmark) (see Figure 4b), the resolution of the CCD cameras was 2048×2048 pixels, and the cameras were equipped with 85 mm and 50 mm f/1.8 Canon lenses. Each camera was installed on a rotating platform to achieve the Scheimpflug state. The laser supply adopted was a dual-power 200 mJ, 15 Hz Nd-Yag laser supplied by Litron Lasers (see Figure 4b). The duration of the laser beam was 4 ns, the laser wavelength 532 nm, and the laser sheet thickness 2 mm. The detailed arrangement of the probes can be found in previous literature [12,36–38].

4.2. Test Details

The experimental setup of the SPIV measurement of the velocity field around the bow of a trimaran is shown in Figure 4. Figure 4a is a photograph of the SPIV setup in the towing tank. Figure 4b displays the schematic diagram of the experimental setup of SPIV and the arrangement of the model and PIV system. Figure 4c shows a close-up of the laser sheet and the field of view (FOV). Figure 4d is a close-up of the position of the testing plane and PIV system. Before measuring the velocity field around the bow, we needed to prepare the test environment (cleaning the water surface and the measurement range envelope area) and the testing model (model reflection treatment), and calibrate SPIV and tracer particle seeding. The SPIV calibration was carried out with a $400 \times 310 \text{ mm}^2$ multilevel dot-matrix Dantec Dynamics calibration target in the measurement area of the towing tank. The water was seeded with neutrally buoyant white polyamide tracer particles (PSP-50 Dantec Dynamics Inc., Skovlunde, Denmark) with an average diameter of $50 \mu\text{m}$ using a self-designed and manufactured particle-seeding device with customized rake-shaped pipes. The calibration and seeding processes have been described in detail in previous studies [12,39–41].

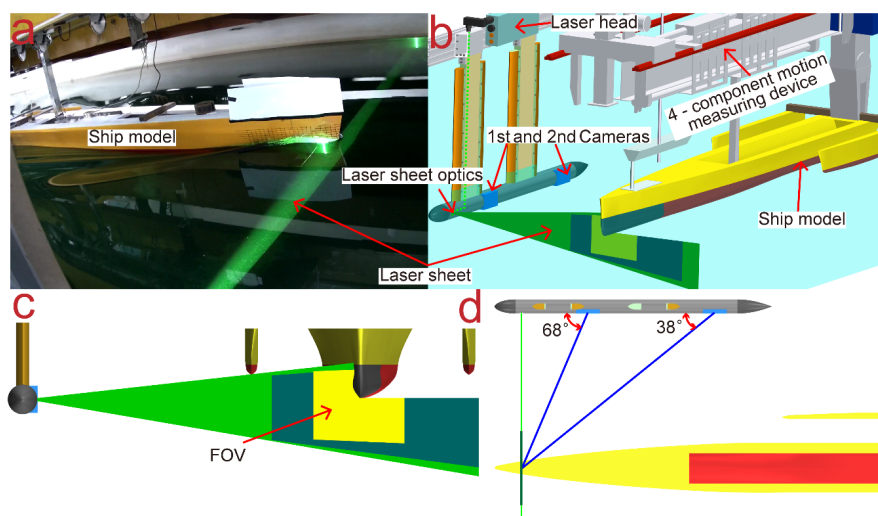


Figure 4. Experimental setup of SPIV measurement: (a) photograph of the SPIV setup in the towing tank, (b) schematic diagram of the SPIV setup, (c) close-up of the laser sheet and the field of view (FOV), and (d) close-up of the position of the testing plane and the PIV system.

The final sinkage and trim of the hull are related to the interaction between the bow and the water mass and the flow tendency of the water particles after flowing through the bow. To accurately adjust the final posture of the testing trimaran, we carried out sinkage and trim measurements of the hull in advance. The detailed experimental values of the sinkage and trim of the testing model are shown in Table 3. Before PIV particle image acquisition, to reduce the influence of the degrees of freedom (DOF) motion of the hull on the image of the PIV measurement area, we adjusted the floating state according to the measured values of the sinkage and trim, after which the DOF motion of the hull was locked.

4.3. Analysis of the Velocity Field

An automatic and adaptive method called the adaptive PIV method was used for calculating velocity vectors based on particle images. The method iteratively adjusts the size and shape of individual interrogation areas (IAs) in order to adapt to local seeding densities and flow gradients (Dantec Dynamics, 2015). In the test, the maximum and minimum sizes of the interrogation areas (IAs) were 64×64 and 32×32 pixels, respectively. The grid step size was 16×16 pixels, and the overlap among neighboring interrogation areas was 50%. Adaptive adjustment applied to each IA iteratively was based on the particle densities and velocity gradients. In the adaptation process, the particle detection limit was that the gray-scale peak must rise 5.0 times above the noise floor and an IA should nominally contain at least 10 particles; the absolute magnitude of the four gradients of U and V in the x - and y -directions should be less than 0.1; and the combined effect of all four gradients should be less than 0.2. The convergence limit and maximum iterations for each adaptive iteration were 0.001 pixel and 10 times the iteration, respectively. The minimum spacing of the vector grid of one velocity vector in the time-averaged velocity map from 250 images per run was $2.45 \times 2.45 \text{ mm}^2$. In this study, the uncertainty and convergence analysis referred to by Falchi et al. [9] and Bendat and Piersol [42,43] was basically the same as that in previous work [39–41], and the detailed uncertainty analysis method and convergence analysis process of the present SPIV are not described again. The distribution of the measurement errors was used to determine a 95% confidence interval that contained the true displacement. The maximum expanded uncertainty of the average velocity with 250 samples at a 95% confidence level was 2.50%.

5. Results and Discussion

5.1. Influence of a Bulbous Bow Type on the Axial Velocity Distribution

Figure 5 shows the dimensionless axial velocity u/U in test plane 1 in the subsurface area ($-0.025 \leq Z/L_{pp} \leq 0.025$) of the bare hull, the bare hull with a small bulbous bow, and the bare hull with a large bulbous bow at a speed of 1.766 m/s; the dimensionless axial velocity u/U in test planes 1 and 2 in the near surface area ($0.02 \leq Z/L_{pp} \leq 0.03$) of the hull are analyzed in Section 5.3. The time-averaged axial velocity u was defined as $u = \frac{1}{250} \sum_{n=1}^{250} u_n$. The time-averaged and towing speeds of the ship model U were dealt with using a dimensionless method. The y - and z -axes were normalized as Y/L_{pp} and Z/L_{pp} .

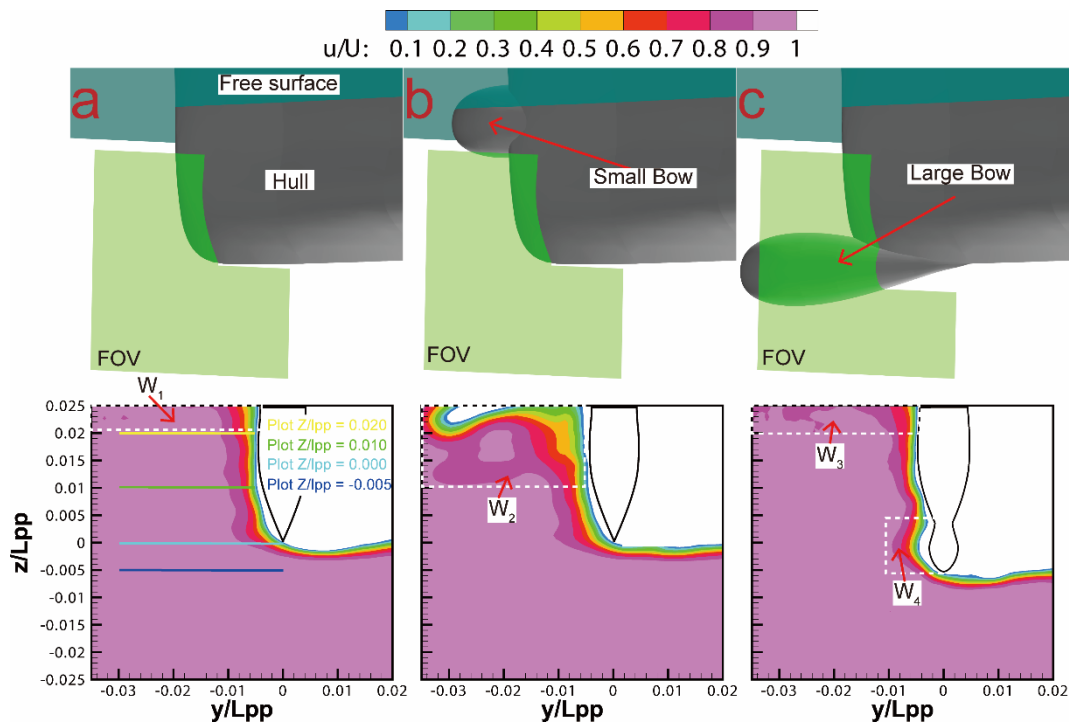


Figure 5. Dimensionless axial velocity u/U in test plane 1 of the testing model at a speed of 1.766 m/s: (a) bare hull, (b) bare hull with a small bulbous bow, and (c) bare hull with a large bulbous bow.

The flow field distribution around the bulbous bow of a ship is mainly affected by the free surface, the horizontal and longitudinal curvature of the hull, and the hydrodynamic appendages installed in the bow. It can be seen from Tables 3 and 4 that at a speed of 1.766 m/s, the difference between the values of sinkage, trim, and local draft at test plane 1 of the bare hull, the bare hull with a small bulbous bow, and the bare hull with a large bulbous bow was small, and the interference of the floating state in the flow field could be ignored. The distribution of the flow field around the bow mainly depends on the contribution of the longitudinal and cross-sectional curvature of the hull. As depicted in Figure 5, the distribution of dimensionless axial velocity u/U was similar to the profile shape of test plane 1 of the bare hull. When the bare hull was equipped with a small bulbous bow, since the midline of the small bulbous bow was in the free surface area, the interaction between the small bulbous bow and the free surface caused a disturbance of the water particles around the bow and a certain range of low-speed wake area (label W_2) was formed behind the small bulbous bow. In addition, the interaction between the bare hull and the free surface had little effect (labels W_1 and W_3) on the flow field around the bow of the bare hull and the bare hull with a large bulbous bow in the subsurface area. Compared with the bare hull, the distribution of the dimensionless axial velocity u/U in the bottom area away from the small bulbous bow was not much different from the dimensionless axial velocity at the bottom of the bare hull. The large bulbous bow was assembled at the baseline of the bare hull. The existence of a large bulbous bow basically had no effect on the distribution of the flow field around the free surface, and it mainly affected the distribution of the flow field around the bottom of the hull in the bow region. The distribution of the dimensionless axial velocity u/U (label W_4) was similar to the profile shape of test plane 1 of the hull with a large bulbous bow.

Figure 6 presents the dimensionless axial velocity u/U in test plane 1 in the subsurface areas of the bare hull, the bare hull with a small bulbous bow, and the bare hull with a large bulbous bow at a speed of 2.943 m/s.

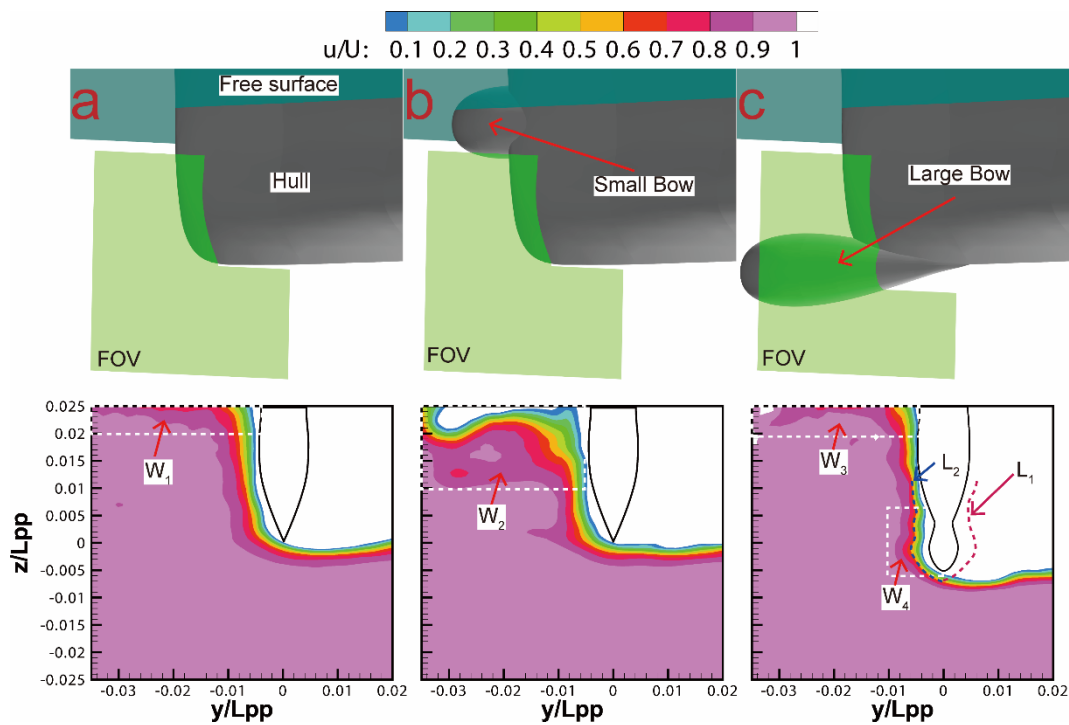


Figure 6. Dimensionless axial velocity u/U in test plane 1 of the testing model at a speed of 2.943 m/s: (a) bare hull, (b) bare hull with a small bulbous bow, and (c) bare hull with a large bulbous bow.

As the speed increased from 1.766 to 2.943 m/s, the influence of the flow field distribution of the bare hull on the free surface gradually increased and a significant disturbance area was generated in the subsurface area. Seo et al. [44] also discovered this phenomenon in the process of measuring the turbulent boundary layer and near wake around a surface-piercing body, near the juncture of the free surface and the model wall, the flow is diminished due to free surface fluctuation and small-scale turbulence production. In addition, the axial velocity distribution was basically the same as the distribution when the speed was 1.766 m/s. The distribution of the flow field around the bow mainly depends on the contribution of the longitudinal and cross-sectional curvature of the hull and the disturbance of the water particles due to the ship bow wave. Under high-speed conditions, the disturbance of the water mass around the bow caused by the interaction between the small bulbous bow and the free surface was more severe, and the low-speed area (label W_2) formed behind the small bulbous bow was larger than that formed at the speed of 1.766 m/s. Since the large bulbous bow was assembled at the baseline of the hull, the hull profile near the free surface area was consistent with the bare hull, and the interaction between the hull and the water mass in the free surface area was basically the same as the effect of the bare hull state, which shows that the near-free-surface area has a significant disturbance area at a speed of 2.943 m/s. As the speed increased, the axial velocity distribution of the large bulbous bow area was still similar to the profile shape of the test-plane-1 hull with the large bulbous bow. However, in the high-speed state, the concave velocity distribution characteristics (labels W_4 and L_2) of the area between the bulbous bow and the hull were gentler than those (label L_1) in the low-speed state.

Figure 7 shows the time-averaged velocity u/U profiles at $Z/Lpp = -0.005, 0.000, 0.010,$ and 0.020 in test plane 1 of the bare hull, the bare hull with a small bulbous bow, and the bare hull with a large bulbous bow; the derivative of the plot or the slope of the tangent of the plot is the velocity gradient in the y-axis direction.

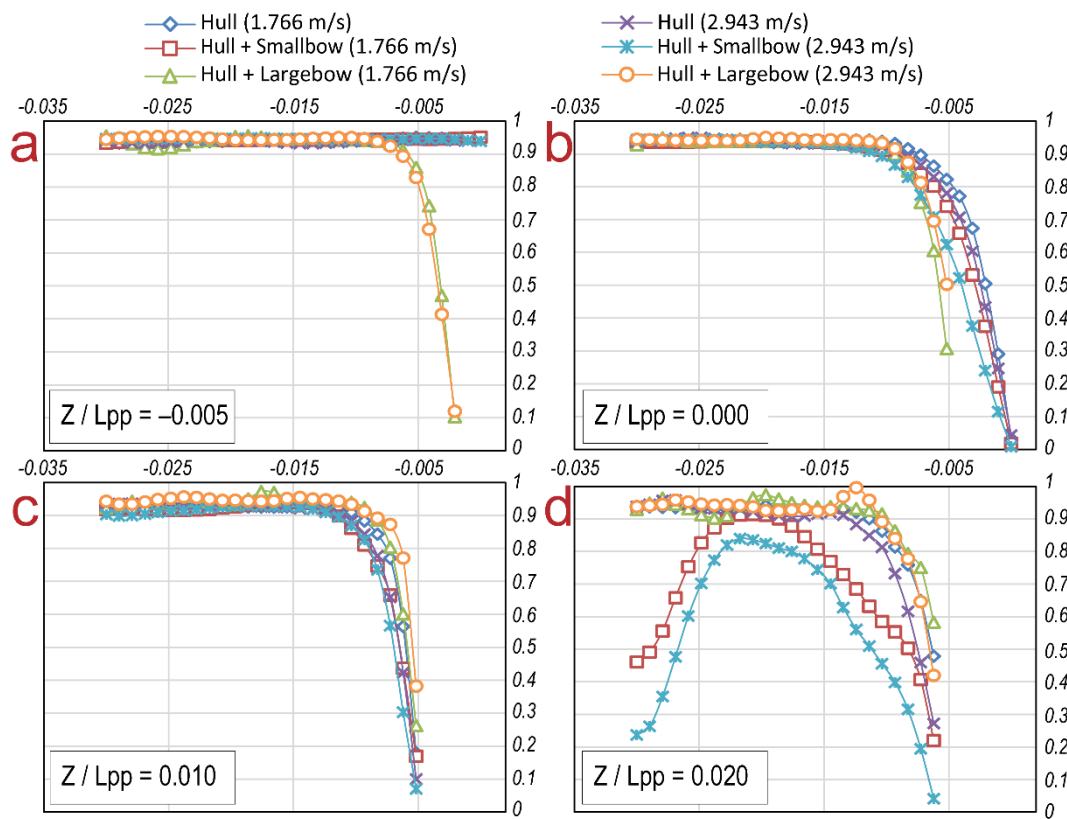


Figure 7. Time-averaged velocity u/U profiles at different Z/L_{pp} lines in test plane 1 of the testing model with different bulbous bows: profiles at Z/L_{pp} = (a) -0.005, (b) 0.000, (c) 0.010, and (d) 0.020.

In the bottom and middle-depth areas of the hull, that is, in the range of $Z/L_{pp} \leq -0.005$ and $-0.005 \leq Z/L_{pp} \leq 0.010$, the overall distribution of axial velocity of the test conditions at a speed of 1.766 m/s was similar to that at a speed of 2.943 m/s. The dimensionless axial velocity u/U profiles at $Z/L_{pp} = -0.005$ of the bare hull and the bare hull with a small bulbous bow showed a flat distribution from $Y/L_{pp} = -0.030$ to 0.000 , and the magnitude of the dimensionless axial velocity u/U was about 0.95. For the bare hull with a large bulbous bow, due to the presence of the bow at the ship’s baseline, the depth of the hull’s disturbance of the water mass was extended. The dimensionless axial velocity u/U profiles at $Z/L_{pp} = -0.005$ of the bare hull with a large bulbous bow showed a flat distribution from $Y/L_{pp} = -0.030$ to -0.015 and a gradually decreasing distribution from $Y/L_{pp} = -0.015$ to -0.000 . The dimensionless axial velocity u/U profiles at $Z/L_{pp} = 0.000$ and 0.010 of the bare hull, the bare hull with a small bulbous bow, and the bare hull with a large bulbous bow showed a flat distribution from $Y/L_{pp} = -0.035$ to -0.015 and a gradually decreasing distribution from $Y/L_{pp} = -0.015$ to -0.000 . In the near-free-surface area of the hull, the dimensionless axial velocity u/U showed an irregular distribution profile from $Y/L_{pp} = -0.030$ to -0.005 . The dimensionless axial velocity u/U profiles at $Z/L_{pp} = 0.020$ of the bare hull and the bare hull with a large bulbous bow showed an oscillatory distribution from $Y/L_{pp} = -0.030$ to -0.015 and a gradually decreasing distribution from $Y/L_{pp} = -0.015$ to -0.005 . The mountain-like distributions of time-averaged velocity u/U first increased from $Y/L_{pp} = -0.035$ to -0.020 then decreased from $Y/L_{pp} = -0.020$ to -0.005 .

5.2. Influence of T Foils on the Axial Velocity Distribution

Figures 8 and 9 display the dimensionless axial velocity u/U in test plane 1 in the subsurface area ($-0.025 \leq Z/L_{pp} \leq 0.025$) of the bare hull with T foils, the bare hull with a small bow and T foils, and the bare hull with a large bow and T foils at speeds of 1.766 and 2.943 m/s. The measurement conditions are relative to those in Section 5.1, but with T foils

installed on the bottom of the bow. Since T foils were installed at a distance behind test plane 1, their contribution to the disturbance of the flow field can be considered negligible in test plane 1. The existence of T foils mainly affects the floating state of the ship in motion, such as sinkage and trim, during stable navigation, and a change in the floating state further affects the encounter state of the forward flow and the bow wave.

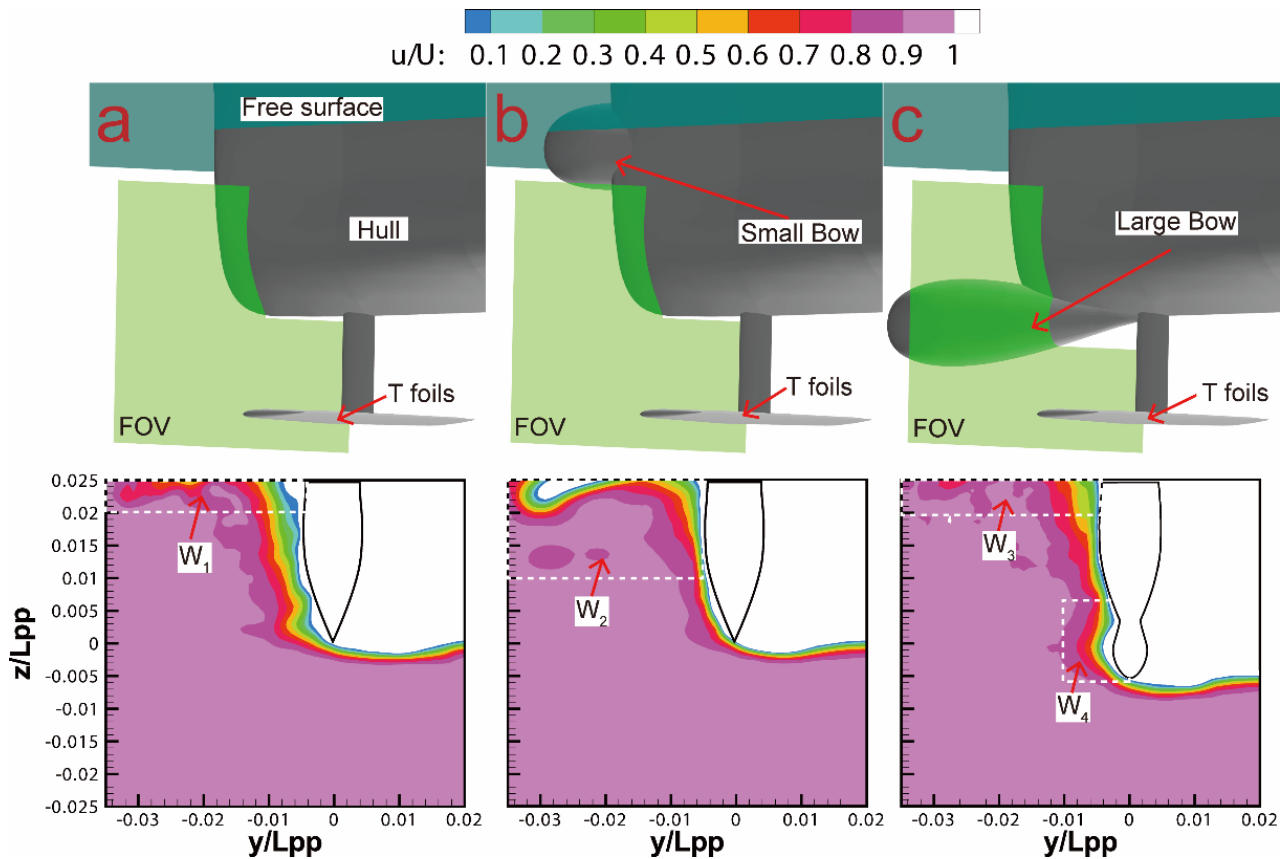


Figure 8. Dimensionless axial velocity u/U in test plane 1 of the testing model with T foils at a speed of 1.766 m/s: (a) bare hull with T foils, (b) bare hull with a small bow and T foils, and (c) bare hull with a large bow and T foils.

It can be seen from Table 4 that the local sinkage values at test plane 1 of the testing model with T foils were deeper than those without T foils. For test conditions at a speed of 1.766 m/s, the testing model was in a bow diving state, and the maximum difference in the local sinkage value was 1.22 mm. On comparing Figures 5 and 8, it can be seen that an increase in the local subsidence value increased the disturbance of the free surface by the ship’s bow. The difference in the flow field between the two working conditions was mainly manifested at the near-free-surface area (labels W_1 , W_2 , and W_3). When the speed increased to 2.943 m/s, except for the working condition of the bare hull with the large bow and T foils, the other working condition of the testing model was the bow raised state, and the maximum difference of the local sinkage value was 2.612 mm. Comparing Figures 6 and 9 showed that the ascent of test plane 1 reduced the disturbance of the free surface by the ship’s bow. The working condition with T foils installed, that is, the working condition with a smaller local positive sinkage value, had a larger range of disturbance to the flow field. Moreover, the concave velocity distribution characteristics of the area between the large bulbous bow and the hull without T foils at the same speed had similar trends (labels L_1 and L_3 at a speed of 1.766 m/s; labels L_2 and L_4 at a speed of 2.943 m/s).

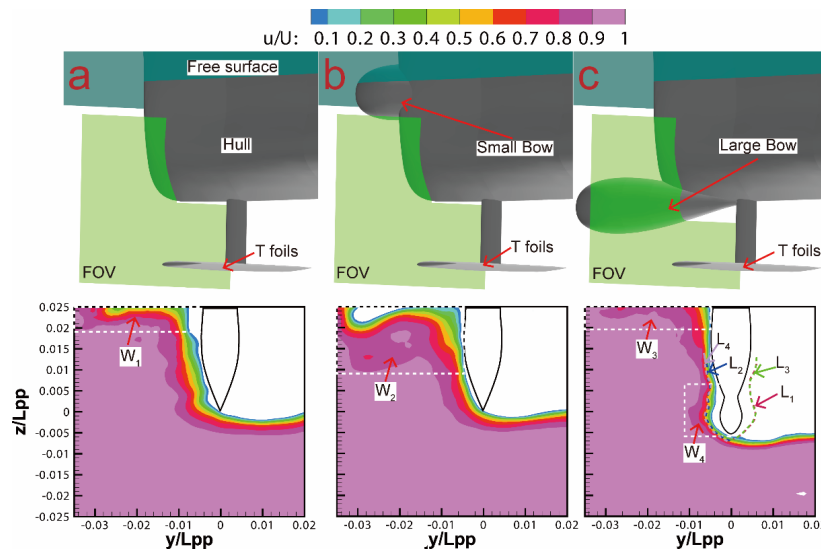


Figure 9. Dimensionless axial velocity u/U in test plane 1 of the testing model with T foils at a speed of 2.943 m/s: (a) bare hull with T foils, (b) bare hull with a small bow and T foils, and (c) bare hull with a large bow and T foils.

Figure 10 presents the time-averaged velocity u/U profiles at $Z/L_{pp} = -0.005, 0.000, 0.010,$ and 0.020 in test plane 1 of the bare hull with T foils, the bare hull with a small bulbous bow and T foils, and the bare hull with a large bulbous bow and T foils. For the bottom and middle-depth areas of the hull, the overall distribution trend of the axial velocity of the hull with T foils was similar to that without T foils. In the near-free-surface area of the hull, for the bare hull with T foils and that with a large bow and T foils, the profiles of axial velocity of the test condition with T foils fluctuated more than those without T foils from $Y/L_{pp} = -0.035$ to -0.015 . For the hull equipped with a small bulbous bow, after installing T foils, the profiles of axial velocity of the test condition at speeds of 1.766 and 2.943 m/s overlapped from $Y/L_{pp} = -0.020$ to -0.005 , and the distribution of other areas was not much different from the conditions without T foils.

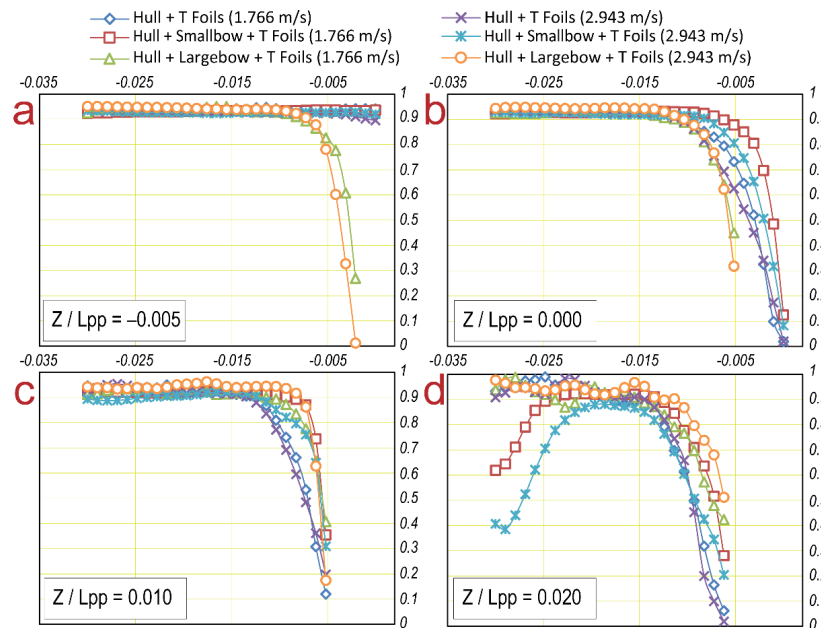


Figure 10. Time-averaged velocity u/U profiles at different Z/L_{pp} lines in test plane 1 of the testing model with T foils and different bulbous bows: profiles at $Z/L_{pp} =$ (a) -0.005 , (b) 0.000 , (c) 0.010 , and (d) 0.020 .

Figure 11 shows the dimensionless axial velocity u/U in test plane 2 in the subsurface area ($-0.025 \leq Z/L_{pp} \leq 0.025$) of the bare hull, the bare hull with T foils, the bare hull with a small bulbous bow and T foils, and the bare hull with a large bulbous bow and T foils at a speed of 1.766 m/s. The wake field distribution at test plane 2 was mainly affected by the line profile of the hull, the stable navigation posture of the ship, and T foils in front of the measurement plane. For the wake field in the range of $0.000 \leq Z/L_{pp} \leq 0.250$, the longitudinal and cross-sectional curvature of the ship were the main factors that affected the flow field. Because the line profiles of test plane 2 in the three working conditions in Figure 11 are the same, the influence of the longitudinal curvature can be ignored. It can also be seen that the longitudinal curvature caused by the small and large bulbous bows had little effect on the flow field in test plane 2. The main reason is that the small bulbous bow is far from test plane 2, and the large bulbous bow at the baseline does not contribute to the disturbance of the upper area. In the bottom area, that is, in the range of $-0.025 \leq Z/L_{pp} \leq 0.000$, the flow field was mainly affected by T foils, the angle of attack change of T foils caused by the stable navigation posture of the ship, and the wake of the large bulbous bow. As shown in Tables 3 and 5, the difference between the sinkage and trim of the ship in different working conditions was small at a speed of 1.766 m/s, where the maximum sinkage difference was 0.419 mm, the maximum trim difference was 0.028° , and the maximum difference of local sinkage at test plane 2 was 1.088 mm. It can be seen from the flow field in the T foil area that the tiny ship-floating-state changes had no effect on the flow field. In addition, because test plane 2 was behind T foils and was affected by T foils, a T-shaped velocity distribution (labels T_1 , T_2 , and T_3) was presented. Due to the synergy of the wake of the large bulbous bow and T foils bracket, the wake after the T foils (label B_1) in Figure 11d is thicker than that in Figure 11a–c.

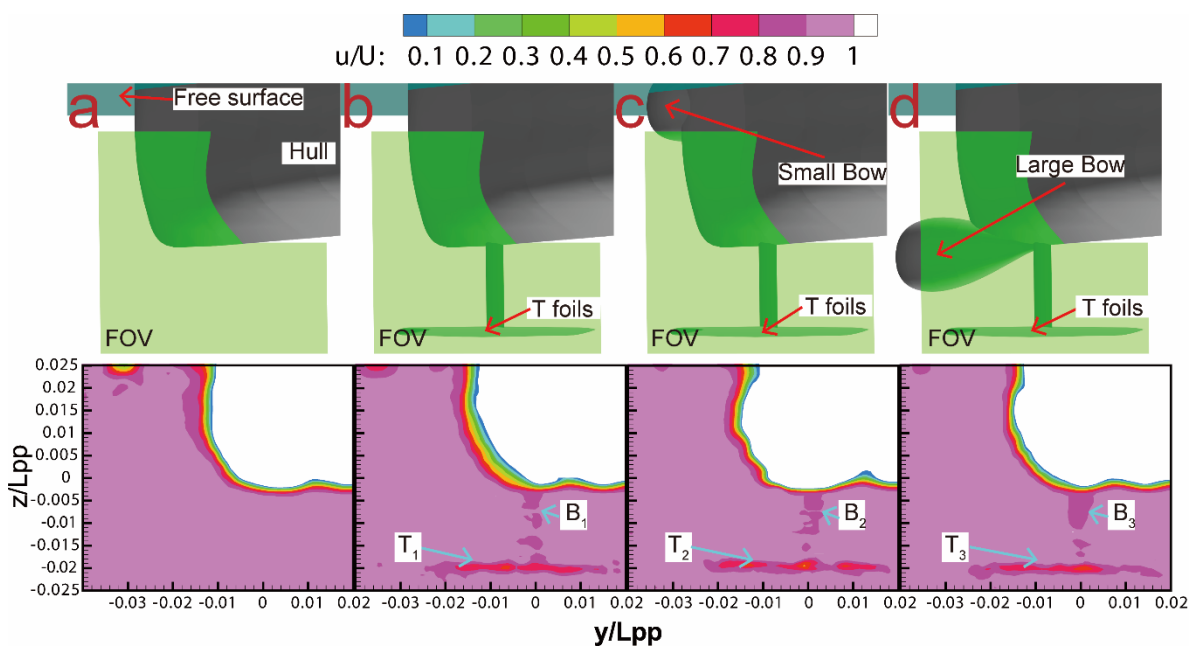


Figure 11. Dimensionless axial velocity u/U in test plane 2 in the subsurface area of the testing model at a speed of 1.766 m/s: (a) bare hull, (b) bare hull with T foils, (c) bare hull with a small bow and T foils, and (d) bare hull with a large bow and T foils.

5.3. Influence of the Bow Wave on the Axial Velocity Distribution

In this subsection, the influence of the bow wave on the axial wake field around the bow is presented. The height and breaking range of the bow wave are important factors that affect the flow field around the bow in the near-free-surface area. Here, the formation, growth, development, and stable evolution of the bow wave are presented. The evolution

diagram of the bow wave is shown in Figure 12, where Figure 12a is the wave-making diagram of the entire region when the ship is sailing stably. Figure 12b–e shows the close-up diagrams of the initial, formation, growth, development, and steady states of the bow wave, respectively.

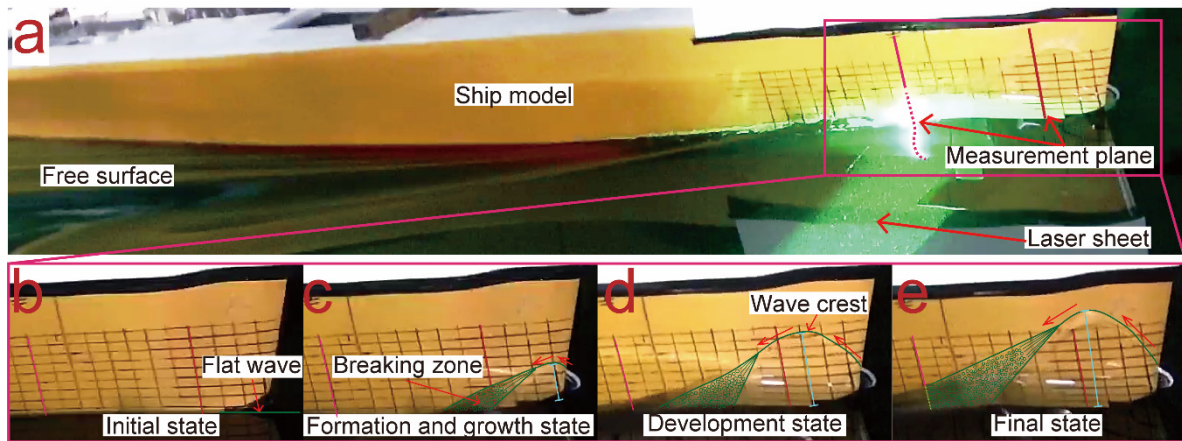


Figure 12. Evolution diagram of the bow wave: (a) wave-making diagram of the entire region when the ship is sailing stably, (b) close-up diagram of the initial state, (c) close-up diagram of the generation and growth states, (d) close-up diagram of the development state, and (e) close-up diagram of the steady state.

As the ship moves from a static floating state, the water mass begins to climb along both sides of the bow due to the squeezing effect of the front edge of the bow. The wave height of the bow gradually climbs and rises over time and reaches the maximum value when the ship is sailing stably. The climbing of the water mass is accompanied by the breaking of the bow wave. The breaking of the bow wave starts in the growth stage and gradually expands away from the bow during the development stage, reaching the maximum range in the stable stage.

The bow wave and the breaking zone around the bow of a trimaran with different appendages are shown in Figure 13.

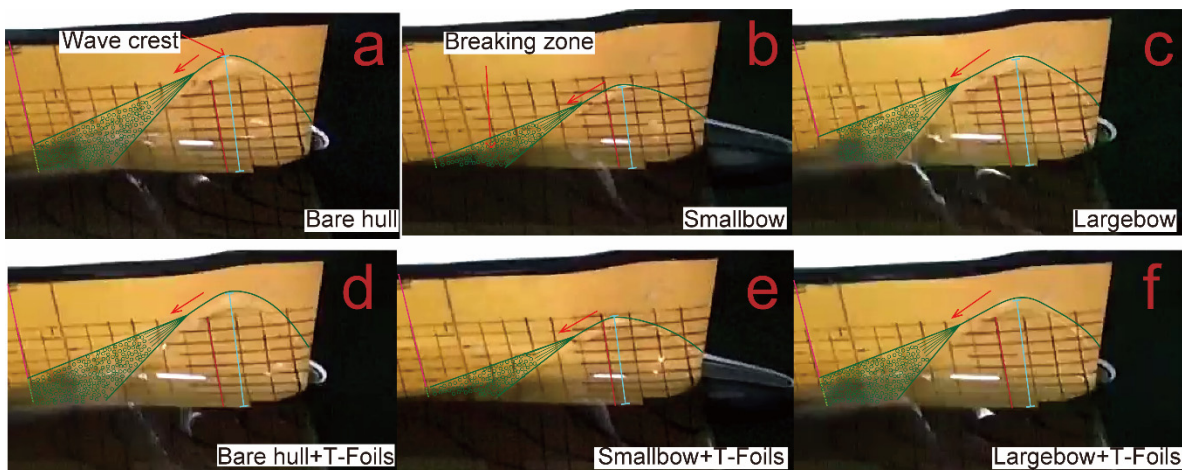


Figure 13. Bow wave and breaking zone around the bow of a trimaran with different appendages: (a) bare hull, (b) bare hull with a small bow, (c) bare hull with a large bow, (d) bare hull with T foils, (e) bare hull with a small bow and T foils, and (f) bare hull with a large bow and T foils.

It can be seen in Figure 13a–f that the range of the breaking wave and the wave height of the bow wave of the small bow state are both the smallest. On the contrary, the wave crest and the wave-breaking range of the bare hull with T foils are the largest. The order of

the height and breaking range of the bow wave is as follows: bare hull with T foils > bare hull > bare hull with a large bow and T foils > bare hull with a large bow > bare hull with a small bow and T foils > bare hull with a small bow. In addition, the heights of the bow waves in the testing condition with T foils attached are all correspondingly higher than those in the testing condition without T foils. The local sinkage value of testing plane-1 in Tables 3 and 4 also confirms this point of view.

Figure 14 displays the dimensionless axial velocity u/U in test plane 1 of the testing model in the near-free-surface area at a speed of 1.766 m/s. As shown in Tables 3 and 4, the locale sinkage at testing plane 1 of the hull with different appendages was not much different. The bare hull with T foils had the largest local sinkage, while the smallest local sinkage was of the bare hull with a small bow, and the maximum difference was 1.239 mm. The height and breaking range of the bow wave are more sensitive to the type of hydrodynamic appendage and local sinkage of the bow. Figure 13 clearly shows the height and breaking range of the bow wave of the hull with different appendages.

Although sinkage values under different working conditions are similar, the difference in the flow fields in test plane 1 of the testing model in the near-free surface area was more obvious due to the influence of bow waves under different working conditions. The overall distribution of the flow field (labels $F_1, F_3, F_4,$ and F_6) in test plane 1 of the bare hull, the bare hull with T foils, the bare hull with a large bow, and the bare hull with a large bow and T foils was similar. The difference was reflected in the range of flow field disturbance caused by the degree of bow wave action, and the range of the perturbed flow field near the free surface of the bare hull with T foils was the largest. For the testing conditions of the bare hull with a small bow and the bare hull with a small bow and T foils, the distribution of the flow field (labels F_2 and F_5) around the hull was quite different from that under other working conditions. This is because the flow field around the free surface area at this time was affected by the coupling effect of the wake field of the bulbous bow and the bow wave.

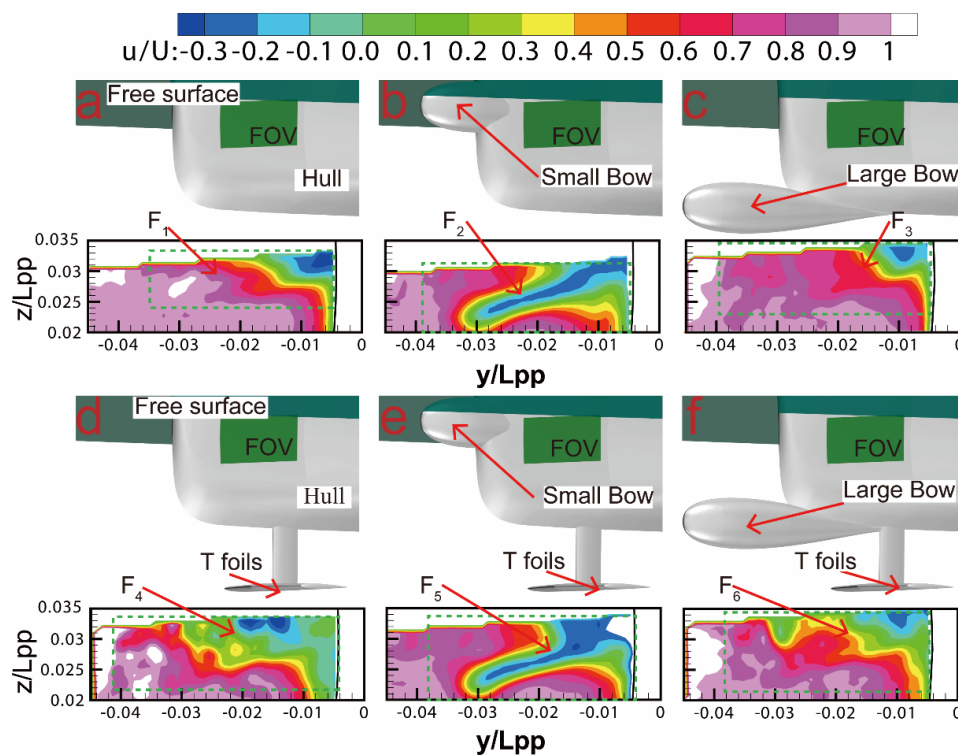


Figure 14. Dimensionless axial velocity u/U in test plane 1 of the testing model in the near-free-surface area at a speed of 1.766 m/s: (a) bare hull, (b) bare hull with a small bow, (c) bare hull with a large bow, (d) bare hull with T foils, (e) bare hull with a small bow and T foils, and (f) bare hull with a large bow and T foils.

Figure 15 presents the dimensionless axial velocity u/U in test plane 2 of the testing model with T foils in the near-free-surface area at a speed of 1.766 m/s.

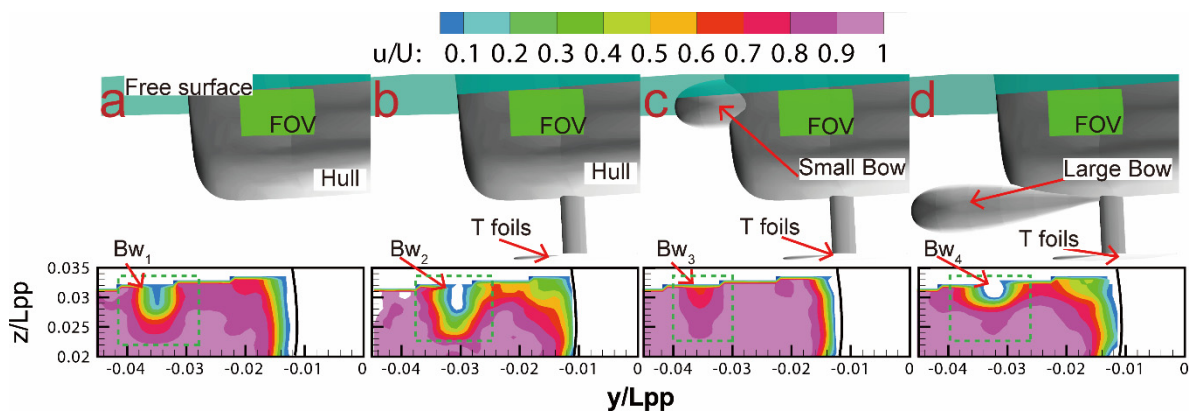


Figure 15. Dimensionless axial velocity u/U in test plane 2 of the testing model in the near-free-surface area at a speed of 1.766 m/s: (a) bare hull, (b) bare hull with T foils, (c) bare hull with a small bow and T foils, and (d) bare hull with a large bow and T foils.

The difference from test plane 1 is that test plane 2 was far away from the appendages in the bow area, where the flow field around the near free surface was mainly affected by the breaking of the bow wave. As shown in Figure 13, the order of the height and breaking range of the bow wave was as follows: bare hull with T foils > bare hull > bare hull with a large bow and T foils > bare hull with a small bow and T foils. In Figure 15, the overall distribution and flow field disturbance range (labels Bw_1 , Bw_2 , Bw_3 , and Bw_4) of the flow field in test plane 2 corresponds to the order of the height and breaking range of the bow wave in Figure 13.

6. Conclusions

In this study, the dimensionless axial velocity u/U in test planes 1 and 2 of a trimaran with different appendages was measured by a towed underwater SPIV system. Based on the flow field of different testing cases, the effects of speed, bulbous bow type, T foils, and bow wave on the axial velocity u/U were studied in detail. The main conclusions are as follows:

- (1) The flow field distribution around the bulbous bow of a ship is mainly affected by the free surface, the horizontal and longitudinal curvature of the hull, and the hydrodynamic appendages installed in the bow. Since the midline of the small bulbous bow is in the free surface area, the interaction between the small bulbous bow and the free surface causes a disturbance of the water particles around the bow and a certain range of low-speed wake area is formed behind the small bulbous bow. In addition, the large bulbous bow has no effect on the distribution of the flow field around the free surface but mainly affects the distribution of the flow field around the bottom of the hull in the bow region.
- (2) Since T foils were installed at a distance behind test plane 1, the contribution of the T foils themselves to the disturbance of the flow field in test plane 1 could be considered negligible. T foils mainly affect the floating state of the ship in motion, such as sinkage and trim, during stable navigation, and a change in the floating state further affects the encounter state of the forward flow and the bow. Comparing Figures 5 and 8, it can be seen that an increase in the local subsidence value increases the disturbance of the free surface by the ship's bow. The difference in the flow field between the two working conditions is mainly manifested at the near free surface. Comparing Figures 6 and 9, it can be seen that the ascent of test plane 1 reduces the disturbance of the free surface by the ship's bow. The working condition with T foils installed,

that is, the working condition with a smaller local positive heave value, has a larger range of disturbance of the flow field.

- (3) The height and breaking range of the bow wave are important factors that affect the flow field around the bow in the near-free-surface area. The climbing of the water mass is accompanied by the breaking of the bow wave, and the breaking of the bow wave starts in the growth stage and gradually expands away from the bow during the development stage, reaching the maximum range in the stable stage. The order of the height and breaking range of the bow wave is as follows: bare hull with T foils > bare hull > bare hull with a large bow and T foils > bare hull with a large bow > bare hull with a small bow and T foils > bare hull with a small bow.
- (4) The overall distribution of the flow field in test plane 1 of a bare hull, a bare hull with T foils, a bare hull with a large bow, and a bare hull with a large bow and T foils was similar. The difference is reflected in the range of flow field disturbance caused by the degree of bow wave action, and the range of the perturbed flow field near the free surface of a bare hull with T foils is the largest. For the testing conditions of a bare hull with a small bow and that with a small bow and T foils, the distribution of the flow field around the hull is quite different from that of other working conditions. This is because the flow field around the free surface area at this time is affected by the coupling effect of the wake field of the bulbous bow and the bow wave. The overall distribution and flow field disturbance range of the flow field in test plane 2 corresponded to the order of the height and breaking range of the bow wave in Figure 13.

Author Contributions: Conceptualization, R.D. and T.W.; methodology, W.L.; software, S.W.; validation, R.D., W.L. and T.W.; formal analysis, S.W.; investigation, S.W.; resources, T.W.; data curation, T.W.; writing—original draft preparation, R.D. and T.W.; writing—review and editing, W.L. and T.W.; visualization, W.L. and T.W.; supervision, R.D. and T.W.; project administration, R.D. and T.W.; funding acquisition, R.D., W.L. and T.W. All authors have read and agreed to the published version of the manuscript.

Funding: Financial support was provided by the Project of Research and Development Plan in Key Areas of Guangdong Province (grant no. 2020B1111010002); the National Natural Science Foundation of China (grant no. 52171330; 52101379; 52101380; 51679053); the Guangdong Basic and Applied Basic Research Foundation (2019A1515110721); the China Postdoctoral Science Foundation (grant no. 2019M663243); the Natural Science Foundation of Guangdong Province, China (2021A1515012134); the Fundamental Research Funds for the Central Universities (no. 2021qntd04); and Opening Fund for State Key Laboratory of Shipping Technology and Security). The APC was funded by the Fundamental Research Funds for the Central Universities (no. 2021qntd04).

Institutional Review Board Statement: Not applicable.

Informed Consent Statement: Not applicable.

Data Availability Statement: The data that support the findings of this study are available within the article.

Conflicts of Interest: The authors declare no conflict of interest.

References

1. Dantec Dynamics. The World's First Towing Tank PIV System. Available online: <https://www.dantecdynamics.com/about/history/> (accessed on 20 July 2021).
2. Gui, L.; Longo, J.; Stern, F. Biases of PIV measurement of turbulent flow and the masked correlation-based interrogation algorithm. *Exp. Fluids* **2001**, *30*, 27–35. [CrossRef]
3. Gui, L.; Longo, J.; Stern, F. Towing Tank PIV Measurement System, Data and Uncertainty Assessment for DTMB Model 5512. *Exp. Fluids* **2001**, *31*, 336–346. [CrossRef]
4. Di Felice, F.; Pereira, F. Developments and Applications of PIV in Naval Hydrodynamics. In *Fluid Mechanics and Its Applications*; Springer Science and Business Media LLC: New York, NY, USA, 2008; Volume 112, pp. 475–503.
5. Yoon, H.S. Phase-Averaged Stereo-PIV Flow Field and Force/Moment/Motion Measurements for Surface Combatant in PMM Maneuvers. Ph.D. Thesis, Department of Mechanical Engineering, The University of Iowa, Iowa City, IA, USA, December 2009.
6. ITTC. Available online: <https://itc.info/media/6087/sc-detailed-flow.pdf> (accessed on 20 July 2021).

7. ITTC. Available online: <https://itc.info/media/5540/15.pdf> (accessed on 20 July 2021).
8. ITTC. Available online: https://itc.info/media/3491/volume2_4wakefield.pdf (accessed on 20 July 2021).
9. Falchi, M.; Felli, M.; Grizzi, S.; Aloisio, G.; Broglia, R.; Stern, F. SPIV measurements around the DELFT 372 catamaran in steady drift. *Exp. Fluids* **2014**, *55*, 1844. [[CrossRef](#)]
10. Yoon, H.; Longo, J.; Toda, Y.; Stern, F. Benchmark CFD validation data for surface combatant 5415 in PMM maneuvers—Part II: Phase-averaged stereoscopic PIV flow field measurements. *Ocean Eng.* **2015**, *109*, 735–750. [[CrossRef](#)]
11. Guo, C.-Y.; Wu, T.-C.; Zhang, Q.; Gong, J. Numerical simulation and experimental research on wake field of ships under off-design conditions. *Ocean Eng.* **2016**, *30*, 821–834. [[CrossRef](#)]
12. Guo, C.-Y.; Wu, T.-C.; Luo, W.-Z.; Chang, X.; Gong, J.; She, W.-X. Experimental study on the wake fields of a Panamax Bulker based on stereo particle image velocimetry. *Ocean Eng.* **2018**, *165*, 91–106. [[CrossRef](#)]
13. Newman, J.N. Flow near the leading edge of a rectangular wing of small aspect ratio with applications to the bow of a ship. *J. Eng. Math.* **1973**, *7*, 163–172. [[CrossRef](#)]
14. Hirata, M.H. The flow near the bow of a steadily turning ship. *J. Fluid Mech.* **1975**, *71*, 283–291. [[CrossRef](#)]
15. Oertel, R. The steady motion of a flat ship including an investigation of local flow near the bow. *Bull. Aust. Math. Soc.* **1976**, *14*, 315–316. [[CrossRef](#)]
16. Grosenbaugh, M.A.; Yeung, R.W. *Flow Structure Near a Ship Bow: An Experimental Investigation*; NAOE-85-1; Department of Naval Architecture and Ocean Engineering, University of California: Berkeley, CA, USA, 1985.
17. Grosenbaugh, M.A.; Yeung, R.W. Flow Structure Near the Bow of a Two-Dimensional Body. *J. Ship Res.* **1989**, *33*, 269–283. [[CrossRef](#)]
18. Fry, D.J.; Kim, Y.H. Bow Flow of Surface Ships. In Proceedings of the 15th Symposium on Naval Hydrodynamics, Hamburg, Germany, 2 June 1985; pp. 319–346.
19. Maruo, H.; Ikehata, M. Some discussions on the free-surface flow around the bow. In Proceedings of the 16th Symposium on Naval Hydrodynamics, Berkeley, CA, USA, 13–18 July 1986; pp. 65–77.
20. Longo, J.; Stern, F.; Toda, Y. Mean-Flow Measurements in the Boundary Layer and Wake and Wave Field of a Series 60 CB = 0.6 Ship Model—Part 2: Scale Effects on Near-Field Wave Patterns and Comparisons with Inviscid Theory. *J. Ship Res.* **1993**, *37*, 16–24. [[CrossRef](#)]
21. Toda, Y.; Stern, F.; Longo, J. Mean-Flow Measurements in the Boundary Layer and Wake and Wave Field of a Series 60 CB = 0.6 Ship Model—Part 1: Froude Numbers 0.16 and 0.316. *J. Ship Res.* **1992**, *36*, 360–377. [[CrossRef](#)]
22. Toda, Y.; Stern, F.; Takana, V.; Patel, V.C. Mean-Flow Measurements in the Boundary Layer and Wake of a Series 60 CB = 0.6 Model Ship with and without Propeller. *J. Ship Res.* **1990**, *34*, 225–252. [[CrossRef](#)]
23. Stern, F.; Longo, J.; Zhang, Z.J.; Subramani, A.K. Detailed Bow-Flow Data and CFD for a Series 60 CB = 0.6 Ship Model for Froude Number 0.316. *J. Ship Res.* **1996**, *40*, 193–199. [[CrossRef](#)]
24. Longo, J.; Stern, F. Effects of drift angle on model ship flow. *Exp. Fluids* **2002**, *32*, 558–569. [[CrossRef](#)]
25. Tahara, Y.; Longo, J.; Stern, F. Comparison of CFD and EFD for the Series 60 CB = 0.6 in steady drift motion. *J. Mar. Sci. Technol.* **2002**, *7*, 17–30. [[CrossRef](#)]
26. Dong, R.R.; Katz, J.; Huang, T.T. On the structure of bow waves on a ship model. *J. Fluid Mech.* **1997**, *346*, 77–115. [[CrossRef](#)]
27. Roth, G.I.; Mascenik, D.T.; Katz, J. Measurements of the flow structure and turbulence within a ship bow wave. *Phys. Fluids* **1999**, *11*, 3512–3523. [[CrossRef](#)]
28. Mallat, B.; Germain, G.; Delacroix, S.; Druault, P. PIV measurements around a bow ship. In Proceedings of the Workshop on Non-Intrusive Measurements for Unsteady Flows and Aerodynamics, Poitiers, France, 27–29 October 2005.
29. Mallat, B.; Germain, G.; Gaurier, B.; Druault, P. Study of the Bubble Sweep-down Phenomenon on Two Ship Models. In Proceedings of the 31th Symposium on Naval Hydrodynamics, Monterey, CA, USA, 11–26 September 2016.
30. Cozijn, J.L.; Hallmann, R. Thruster-Interaction Effects on a DP Shuttle Tanker-Wake Flow Measurements of the Main Propeller and Bow Tunnel Thrusters. In Proceedings of the 33rd International Conference on Ocean, Offshore and Arctic Engineering, San Francisco, CA, USA, 1 June 2014.
31. Yoon, H.; Gui, L.; Bhushan, S.; Stern, F. Tomographic PIV Measurements For Surface Combatant 5415 Straight Ahead and Static Drift 10 and 20 Degree Conditions. In Proceedings of the 30th Symposium on Naval Hydrodynamics, Hobart, TAS, Australia, 2–7 November 2014.
32. Bhushan, S.; Yoon, H.; Stern, F.; Guilmiuau, E.; Visonneau, M.; Toxopeus, S.; Simonsen, C.; Aram, S.; Kim, S.E.; Griporopoulos, G.; et al. CFD Validation for Surface Combatant 5415 Straight Ahead and Static Drift 20 Degree Conditions. Presented at the SNAME 5th World Maritime Technology Conference, Providence, RI, USA, 3–7 November 2015.
33. Bhushan, S.; Yoon, H.; Stern, F. Large grid simulations of surface combatant flow at straight-ahead and static drift conditions. *Int. J. Comput. Fluid Dyn.* **2016**, *30*, 356–362. [[CrossRef](#)]
34. Jacobi, G.; Thill, C.H.; Huijsmans, R.H.M. Pressure reconstruction from velocity field measurements obtained with particle image velocimetry in the bow region of a fast ship. In Proceedings of the 6th International Conference on Advanced Model Measurement Technology for The Maritime Industry AMT'19, Rome, Italy, 9–11 October 2019.
35. Deng, R.; Luo, F.; Wu, T.; Chen, S.; Li, Y. Time-domain numerical research of the hydrodynamic characteristics of a trimaran in calm water and regular waves. *Ocean Eng.* **2019**, *194*, 106669. [[CrossRef](#)]

36. Kandasamy, M.; Wu, P.C.; Zalek, S.; Karr, D.; Bartlett, S.; Nguyen, L. CFD based Hydrodynamic Optimization and Structural Analysis of the Hybrid Ship Hull. In Proceedings of the SNAME Annual Meeting and Expo and Ship Production Symposium, Houston, TX, USA, 22–24 October 2014.
37. Peltzer, T.J.; Keipper, T.S.; Kays, B.; Shimozono, G. A New Paradigm for High-Speed Monohulls: The Bow Lifting Body Ship. Available online: <https://citeseerx.ist.psu.edu/viewdoc/download?doi=10.1.1.482.7035&rep=rep1&type=pdf> (accessed on 20 July 2021).
38. Zong, Z.; Sun, Y.; Jiang, Y. Experimental study of controlled T-foil for vertical acceleration reduction of a trimaran. *J. Mar. Sci. Technol.* **2018**, *24*, 553–564. [[CrossRef](#)]
39. Luo, W.; Guo, C.; Wu, T.; Xu, P.; Su, Y. Experimental study on the wake fields of a ship attached with model ice based on stereo particle image velocimetry. *Ocean Eng.* **2018**, *164*, 661–671.
40. Wu, T.; Luo, W.; Jiang, D.; Deng, R.; Li, Y. Stereo Particle Image Velocimetry Measurements of the Wake Fields Behind A Panamax Bulker Ship Model Under the Ballast Condition. *J. Mar. Sci. Eng.* **2020**, *8*, 397. [[CrossRef](#)]
41. Wu, T.C.; Deng, R.; Luo, W.Z.; Sun, P.N.; Dai, S.S.; Li, Y.L. 3D-3C wake field measurement, reconstruction and spatial distribution of a Panamax Bulk using towed underwater 2D–3C SPIV. *Appl. Ocean Res.* **2020**, *105*, 102437. [[CrossRef](#)]
42. Bendat, J.S.; Piersol, A.G. *Random Data—Analysis and Measurement Procedures*, 2nd ed.; John Wiley & Sons, Inc.: Hoboken, NJ, USA, 1986.
43. Bendat, J.S.; Piersol, A.G. *Random Data—Analysis and Measurement Procedures*, 4th ed.; John Wiley & Sons, Inc.: Hoboken, NJ, USA, 2010.
44. Dong, M.S.; Jeong, H.S.; Shin, H.R. Towed underwater PIV measurement for free-surface effects on turbulent wake of a surface-piercing body. *Int. J. Nav. Archit.* **2013**, *5*, 404–413.